ARTICLES
https://doi.org/10.1038/s41557-020-00635-5
nature chemistry

Check for updates

Metal–organic frameworks embedded in a liposome facilitate overall photocatalytic water splitting

Huihui Hu[1], Zhiye Wang[1], Lingyun Cao[1], Lingzhen Zeng[1], Cankun Zhang[1], Wenbin Lin[2] and Cheng Wang[1]✉

Metal–organic frameworks (MOFs) have been studied extensively in the hydrogen evolution reaction (HER) and the water oxidation reaction (WOR) with sacrificial reagents, but overall photocatalytic water splitting using MOFs has remained challenging, principally because of the fast recombination of photo-generated electrons and holes. Here we have integrated HER- and WOR-MOF nanosheets into liposomal structures for separation of the generated charges. The HER-MOF nanosheets comprise light-harvesting Zn–porphyrin and catalytic Pt–porphyrin moieties, and are functionalized with hydrophobic groups to facilitate their incorporation into the hydrophobic lipid bilayer of the liposome. The WOR-MOF flakes consist of [Ru(2,2′-bipyridine)$_3$]$^{2+}$-based photosensitizers and Ir–bipyridine catalytic centres, and are localized in the hydrophilic interior of the liposome. This liposome–MOF assembly achieves overall photocatalytic water splitting with an apparent quantum yield of (1.5 ± 1)% as a result of ultrafast electron transport from the antennae (Zn–porphyrin and [Ru(2,2′-bipyridine)$_3$]$^{2+}$) to the reaction centres (Pt–porphyrin and Ir–bipyridine) in the MOFs and efficient charge separation in the lipid bilayers.

The construction of artificial chloroplasts has been a long-held goal for chemists[1]. Natural photosynthesis takes place on thylakoid membranes in chloroplasts where protein complexes for light harvesting, charge separation and catalysis are grouped into photosystem I for nicotinamide adenine dinucleotide phosphate ($NADP^+$) reduction and photosystem II for water oxidation[2]. The electrons are pumped twice using two separate photons at the two photosystems, giving a 'zig-zag' energy profile of the electrons in a so called 'Z-scheme' to overcome the high overpotentials of the reactions[3,4]. The thylakoid membrane spatially separates the generated charges and prevents their recombination to ensure a high solar-to-chemical conversion efficiency.

The 'Z-scheme' of photon management and the spatial separation of the two half-reactions have also been employed in artificial photosynthesis for solar fuel production. For example, light-driven overall water splitting to hydrogen and oxygen has been achieved in colloidal semiconductor/catalyst assemblies, integrated photo-electrochemical cells and hybrid photobiochemical systems[5–11]. Although MOFs built from photo-active molecular units have provided a versatile platform for studying the key steps of artificial photosynthesis, such as the WOR and the HER[12–17], few MOF-only systems have been used for overall photocatalytic water splitting, due to the inability of spatially separating light-generated charges to prevent recombination. The charge recombination also sets limits on other MOF-based photocatalytic processes including CO_2 reduction and synthetically useful organic transformations. With lipid bilayers mimicking biological membranes, liposomes have provided a scaffold for the construction of biomimetic structures for charge separation and solar energy harvesting[18–22]. We posit that liposomal structures could provide a strategy for organizing WOR-MOFs and HER-MOFs to achieve overall water splitting.

Among molecular catalytic centres for the HER half-reaction, [(TCPP)Pt], where TCPP = meso-tetra(4-carboxyphenyl)porphine, shows a very high turnover frequency (TOF) of 35 h^{-1} (ref. [23]). As the HER requires two photon-generated electrons, it is critical to transport two equivalents of excited states or electrons to the same catalytic centre within a short time interval. We have achieved this by constructing a MOF antenna: hafnium-based nodes are used for framework stability, and light-harvesting [(TCPP)Zn]-based ligands doped with [(TCPP)Pt] moieties allow fast energy/electron transfer from the [(TCPP)Zn] network to the reaction centre of the [(TCPP)Pt] moieties. The four-connected $Hf_6(\mu_3\text{-}O)_4(\mu_3\text{-}OH)_4$ nodes and four-connected [(TCPP)Zn]/[(TCPP)Pt] ligands formed a two-dimensional network of square lattice (sql) topology. For the WOR half-reaction, Ir–BPY complexes[24] (BPY = 2,2′-bipyridine) as the reaction centres were incorporated within a [Ru(BPY)$_3$]$^{2+}$-based MOF to act as antennae to allow efficient energy/hole transfer from [Ru(BPY)$_3$]$^{2+}$ to Ir–BPY. Zirconium-based nodes instead of hafnium-based nodes were chosen for the construction of stable WOR-MOFs, to differentiate them from the HER-MOFs and for easier quantification of these two MOFs in the final assembly. The $Zr_{12}(\mu_3\text{-}O)_8(\mu_3\text{-}OH)_8(\mu_2\text{-}OH)_6$ nodes were connected by Ru- or Ir-based dicarboxylate ligands to form a hexagonal close-packed structure.

The HER- and WOR-MOF nanosheets were then assembled in the hydrophobic and hydrophilic regions, respectively, of liposome (LP) vesicles constructed from lecithin (PC) and cholesterol (Chol) in a molar ratio of 3:1 for overall photocatalytic water splitting (Fig. 1). The HER-MOF is of monolayer thickness and functionalized with hydrophobic pentafluoropropionate groups for insertion into the hydrophobic region of the lipid bilayer, whereas the WOR-MOF nanosheets are assembled in the interior of the liposome. The HER-MOF and the WOR-MOF are connected by two redox relays—the tetrachlorobenzoquinone/tetrachlorobenzohydrosemiquinone (TCBQ/TCBQH) pair, introduced into the lipid bilayer in the organic phase before film formation, and the Fe^{3+}/Fe^{2+} pair, introduced into the aqueous phase in the hydration step—that carry out the electron-transfer processes. The lipid membrane

[1]Collaborative Innovation Center of Chemistry for Energy Materials, State Key Laboratory of Physical Chemistry of Solid Surfaces, Department of Chemistry, College of Chemistry and Chemical Engineering, Xiamen University, Xiamen, P.R. China. [2]Department of Chemistry, The University of Chicago, Chicago, IL, USA. ✉e-mail: wangchengxmu@xmu.edu.cn

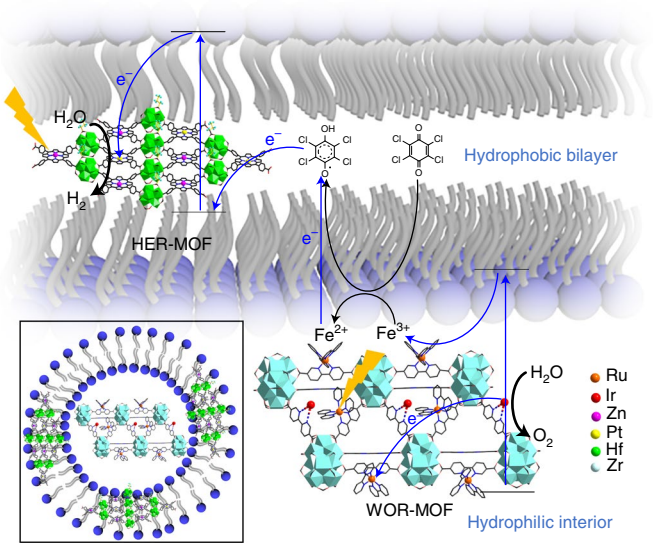

Fig. 1 | Structure of the LP–MOF for overall photocatalytic water splitting and the proposed 'Z-scheme' electron-transfer chain in the LP–MOF system. The bilayer in the illustration represents a section of the liposome. The HER-MOF for hydrogen evolution is incorporated between the hydrophobic chains, and the WOR-MOF for water oxidation is in the aqueous phase. Both MOFs are represented by polyhedron–ball–stick models; see Fig. 2 for their structures. The redox shuttles TCBQ/TCBQH and Fe^{3+}/Fe^{2+} connect the HER and WOR sides, functioning in the lipid phase and the aqueous phase, respectively. Electron-transfer chains (shown by blue arrows) and photons (represented by yellow lightning shapes) form the 'Z-scheme'. Inset, schematic representation of the liposome with the two MOFs embedded within the hydrophobic bilayer (HER-MOF) and the hydrophilic interior (WOR-MOF).

separates light-generated reductive species like [(TCPP)Pt-H] for HER and oxidative species like $[Ru(BPY)_3]^{3+}$ for WOR on the two MOFs. For the HER-MOF, light-induced charge separation between [(TCPP)Zn] and [(TCPP)Pt] generates $[(TCPP)Zn]^+$ and $[(TCPP)Pt]^-$. $[(TCPP)Pt]^-$ is then protonated to [(TCPP)Pt-H] before accepting another electron and another proton to release one H_2, while $[(TCPP)Zn]^+$ reacts with TCBQH to regenerate [(TCPP)Zn] and give TCBQ that oxidizes Fe^{2+} to Fe^{3+} at the lipid/water interface. The WOR-MOF is initiated by the photo-oxidation of $[Ru(BPY)]^{2+*}$ by the Fe^{3+} to produce $[Ru(BPY)]^{3+}$, which in turn oxidizes the Ir–BPY complex for water oxidation. This LP–MOF assembly mimics natural photosynthetic systems for light-to-chemical conversion.

Results and discussion

Preparation of the LP–MOF assemblies. The HER-MOF is constructed from metalloporphyrin ligands [(TCPP)Zn] and [(TCPP)Pt] (see Supplementary Figs. 1–3) and $Hf_6(\mu_3\text{-}O)_4(\mu_3\text{-}OH)_4$ secondary building units (SBUs) (Fig. 2a and Supplementary Figs. 5 and 6). Nanosheets with a lateral size of less than 200 nm were obtained from solvothermal synthesis by intentionally adding water to a mixed solvent of dimethylformamide (DMF) and formic acid (HCO_2H) (Fig. 3a) followed by sonication and filtration through a porous membrane (1 μm) to make the MOF particles smaller and remove the larger flakes (Supplementary Fig. 7a)[25–28]. High-resolution transmission electron microscopy (HRTEM) (Supplementary Fig. 7b) and scanning transmission electron microscopy-high angle annular dark-field (STEM-HAADF) images (Fig. 3b and Supplementary Fig. 7c) showed an sql lattice that matches the structural model of a two-dimensional layer of alternately connected TCPP ligands and Hf_6 SBUs (Fig. 3b). This structural assignment was confirmed by powder X-ray diffraction (PXRD) studies (Supplementary Fig. 8) and chemical composition analysis (Supplementary Figs. 9 and 10). Atomic force microscopy (AFM) gave a range of thickness of 1.3–2.2 nm, roughly matching the height of a flat or zig-zag layer (Fig. 3c and Supplementary Fig. 11). HER-MOFs have chemical compositions of $[Hf_6(\mu_3\text{-}O)_4(\mu_3\text{-}OH)_4(\mu_1\text{-}OH)_2(\mu_1\text{-}H_2O)_2(HCO_2)_6[(TCPP)Zn]_{1-x}[(TCPP)Pt]_x]$.

The WOR-MOF was constructed from the $Zr_{12}(\mu_3\text{-}O)_8(\mu_3\text{-}OH)_8(\mu_2\text{-}OH)_6$ SBU and $[Ru^{II}(BPY)_2(BPYDC)]$ (abbreviated as $[Ru]^{2+}$, where BPYDC are 2,2′-bipyridine-5,5′-dicarboxylic acid bridging ligands) (Supplementary Fig. 4) with a BPYDC/$[Ru]^{2+}$ ratio of 1.7 as determined by proton NMR of digested MOF (Supplementary Fig. 12). Further functionalization with Ir^{III} gave [(BPYDC)Ir] catalytic centres (Fig. 2b) that are evenly distributed in the MOF, as shown by energy dispersive X-ray spectroscopy images (Supplementary Fig. 13)[26,29]. The MOF without an Ir centre is denoted as Zr-$[Ru]^{2+}$-MOF, while the one with Ir is denoted as WOR-MOF. The WOR-MOF exhibits a hexagonal nanoplate morphology with a thickness range of 1.2–11.5 nm, as measured by AFM (Fig. 3f and Supplementary Fig. 14), and a lateral size of the order of 400 nm, as measured by TEM (Fig. 3d and Supplementary Figs. 15 and 16). HRTEM (Fig. 3e) and PXRD (Supplementary Fig. 17) studies confirm that WOR-MOFs adopt a 'double-decker' hexagonal close-packed structure[29,30], in which six lateral connections on each Zr_{12} node are through double bridges of two parallel dicarboxylate linkers (Fig. 2b).

The HER-MOF was treated with pentafluoropropionic acid to give a hydrophobic surface by replacing the formate capping groups on the SBU. This hydrophobic modification was confirmed by a change in the water contact angle from 65 ± 2° to 136 ± 3° (Supplementary Fig. 18). We incorporated the HER-MOF into the lipid bilayer by adding the nanosheets to the lecithin/cholesterol mixture in the preparation of the liposome assembly (LP–HER-MOF)[31]. Thicker HER-MOFs were not incorporated into the bilayer and were removed in an extrusion step as they tended to aggregate outside the liposome to form large particles, leading to an incorporation yield of (4 ± 2)% for the HER-MOF (Supplementary Fig. 19). The redox shuttle TCBQ was also added to the lipid bilayer. The lipid mixture first formed a film on wall of the flask (Fig. 4a) and was then hydrated and sonicated to form small vesicles. The WOR-MOF nanosheets and the redox shuttle Fe^{3+} ions were introduced into the aqueous phase in the hydration step (LP–WOR-MOF). Interactions between the polar phosphate head groups of the lipids and the cationic WOR-MOF and Fe^{3+} ions help to increase their chances of being wrapped inside the liposome, leading to a wrapping yield of (2.6 ± 1)% for the WOR-MOF. Most of the WOR-MOFs outside the liposome were removed in the extrusion step because of their aggregation into large particles.

The diameters of the LP–HER-WOR-MOF were 2 ± 0.5 μm as determined by dynamic light scattering and TEM imaging (Fig. 4h and Supplementary Figs. 20–24). The TEM images also showed WOR-MOF nanosheets (Supplementary Figs. 23 and 24) but were insensitive to HER-MOF in the lipid bilayer.

We also used fluorescence confocal microscopy to locate the HER-MOF and WOR-MOF in the liposomes. In the image of the LP–HER-MOF, [(TCPP)Zn] fluorescence clearly showed as ring-like structure when the liposome was right at the focus (Supplementary Figs. 25 and 26), which is consistent with the HER-MOF being located within the lipid bilayer. In the image of the LP–WOR-MOF, $[Ru]^{2+}$ phosphorescence appeared only in the inner part of the liposome (Supplementary Fig. 27). In the LP–HER-WOR-MOF hybrid, owing to spectral overlap between the two MOFs, it is difficult to assign one channel to a specific MOF, but excitation at 488 nm led to more signal from the WOR-MOF, while excitation at 552 nm led to more signal from the HER-MOF (Fig. 4j). The signal responsible for the WOR-MOF seems to be from the inner part

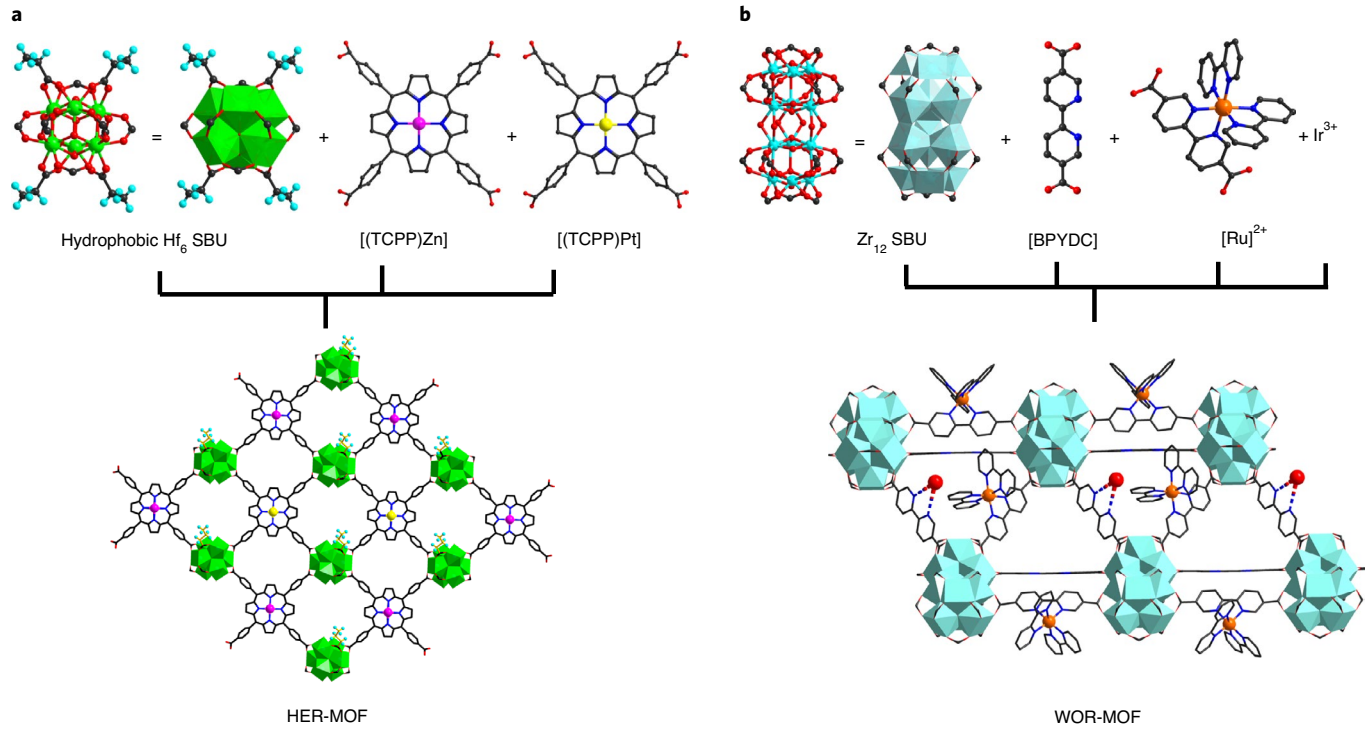

Fig. 2 | HER-MOF and WOR-MOF structures. a, HER-MOF constructed from hydrophobically modified $Hf_6(\mu_3\text{-}O)_4(\mu_3\text{-}OH)_4$ clusters with pentafluoropropionate groups and [(TCPP)Zn]/[(TCPP)Pt] linkers. $Hf_6(\mu_3\text{-}O)_4(\mu_3\text{-}OH)_4(\mu_1\text{-}OH)_2(\mu_1\text{-}H_2O)_2(HCO_2)_6$ clusters are shown as green polyhedra; Zn atoms in the centre of [(TCPP)Zn] are shown in purple; Pt atoms in the centre of [(TCPP)Pt] are in yellow. **b**, WOR-MOF constructed from $Zr_{12}(\mu_3\text{-}O)_8(\mu_3\text{-}OH)_8(\mu_2\text{-}OH)_6$ clusters and $[Ru]^{2+}$ and [BPYDC] linkers. Some of the [BPYDC] were functionalized with Ir^{3+}. $Zr_{12}(\mu_3\text{-}O)_8(\mu_3\text{-}OH)_8(\mu_2\text{-}OH)_6$ clusters are shown as sky blue polyhedral; Ru atoms in the centre of $[Ru^{II}(BPY)_2(BPYDC)]$ are in orange; Ir in [(BPYDC)Ir] are in red. In both structures: C, grey; N, blue; H omitted for clarity.

of the liposome, whereas the channel assigned to the HER-MOF showed a higher intensity on the shell (Fig. 4b–g, Supplementary Fig. 28). We also observed complete signal overlap in some of the liposomes, which may be due to the formation of multilamellar vesicles. Furthermore, phosphorescence from the Zr-$[Ru]^{2+}$-MOF can be efficiently quenched by water-soluble Fe^{3+} but not by lipid-soluble TCBQ (Supplementary Fig. 29), confirming its location in the aqueous phase inside the liposome (Fig. 4i). Similarly, the fluorescence of the Hf-[(TCPP)Zn]-MOF cannot be quenched by Fe^{3+} in the aqueous phase but can by lipid-soluble TCBQ when it is incorporated into the liposomal structure (Fig. 4i and Supplementary Figs. 30 and 31).

The amounts of encapsulated MOFs in the LP–HER-WOR-MOF hybrid were determined using inductively coupled plasma-mass spectrometry (ICP-MS), and showed a molar ratio for PC/Chol/HER-MOF/WOR-MOF/TCBQ/Fe^{3+} of $696:230:(8.5\pm3.8):(2\pm0.8)$:22:24 (where the MOFs are counted by the number of SBUs, and the ligand/SBU ratios are equal to one in the HER-MOF and nine in the WOR-MOF) and 696:230:9:2:22:24 for a typical sample used in the water-splitting test. Variations exist among different samples. The molar ratio of Pt/Zn in the HER-MOF was 0.011 and the molar ratio of Ir/Ru in the WOR-MOF was 0.82. These ratios were chosen based on different energy-/electron-transfer efficiencies in these two systems to optimize catalytic activities. The functionalized liposome was then examined for overall photocatalytic water splitting.

Photocatalytic hydrogen evolution. The HER-MOF and the LP–HER-MOF hybrid were first tested for the HER half-reaction under irradiation by a 400 nm light-emitting diode (LED) using phenol as a sacrificial agent. The amount of hydrogen evolved in the headspace of the vial was quantified by gas chromatography (GC) and the amounts of encapsulated MOFs in the LP–HER-MOF were determined using ICP-MS (Supplementary Table 1). The TOF, as calculated by the molar ratio of generated H_2 to [(TCPP)Pt] in 24 h, was approximately $1.25\times10^4\,h^{-1}$, and is among the highest reported for molecular systems (Supplementary Table 2)[32–37]. The bare HER-MOF assembly without liposome showed a comparable TOF of $1.2\times10^4\,h^{-1}$ (Supplementary Table 2). A MOF without [(TCPP)Pt] and the sacrificial agent (phenol) did not show any HER activity, confirming [(TCPP)Pt] as the catalytic centre and excluding the possibility that a blank liposome can serve as a sacrificial agent (Supplementary Table 3). The Pt-based TOF was inversely related to the ratio of [Zn]/([Pt] + [Zn]) (Fig. 5a), showing the importance of [(TCPP)Zn] as an antenna.

After catalysis, the [(TCPP)Pt] and [(TCPP)Zn] moieties remained intact, as shown by the characteristic [(TCPP)Zn] peaks in the UV-visible absorption spectra of the HER-MOF before and after the reaction (Supplementary Fig. 32). The HER-MOF structure was also stable under the reaction conditions used here, as revealed by the retention of its PXRD pattern (Supplementary Figs. 33–35).

Photocatalytic water oxidation. The WOR-MOF and LP–WOR-MOF hybrid were tested for the WOR half-reaction under irradiation by a 450 nm LED. Amount of oxygen evolved was quantified using both GC and a fluorescent probe (YSI ProODO) in the aqueous phase (Fig. 5b). The LP–WOR-MOF showed steady oxygen generation for 12 h using $Na_2S_2O_8$ as the sacrificial agent to afford a TOF of $25\,h^{-1}$, which is comparable to other efficient

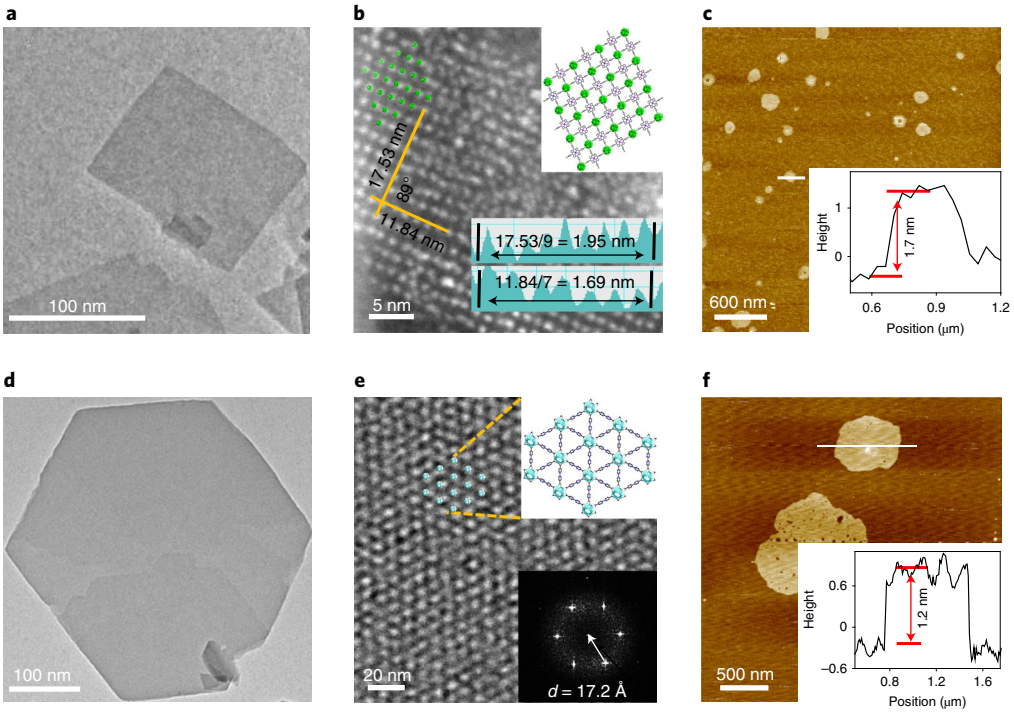

Fig. 3 | Preparation and characterization of HER-MOF and WOR-MOF. a, TEM image of HER-MOF. **b**, STEM-HAADF image of HER-MOF showing a rectangular arrangement of SBUs (white dots). The measured inter-SBU distances in the HAADF image were 1.69 nm in one direction (1.67 nm in the model, with 1% deviation) and 1.95 nm in the other direction (1.97 nm in the model, with 1% deviation), matching that of the zig-zag monolayer HER-MOF model in the inset, which is also superimposed on the upper left corner of the image. **c**, AFM image of HER-MOF with the height profile in the inset, which is measured along the white line on the image. **d**, TEM image of WOR-MOF. **e**, HRTEM images of WOR-MOF showing a hexagonal arrangement of SBUs (dark dots), with a structural model superimposed on the image, and a Fourier transform of the image for extracting the distance between the lines of SBUs at 1.72 nm. **f**, AFM image of WOR-MOF with the height profile in the inset, which is measured along the white line on the image.

photocatalytic molecular catalysts (Supplementary Tables 4 and 5 and Supplementary Figs. 36–39)[38–40]. The bare WOR-MOF assembly without any liposome showed a similar TOF of 21 h^{-1} (Supplementary Table 4).

Overall photocatalytic water splitting. We then combined the HER and WOR parts in the LP–HER-WOR-MOF assembly for overall water splitting with the redox shuttles TCBQ in the lipid bilayer, introduced in the organic phase before film formation, and Fe^{3+} in the aqueous phase, introduced in the hydration step. Hydrogen and oxygen were detected in a roughly 2:1 ratio under LED illumination (Fig. 5c). The MOFs inside the assembled liposome were stable during the catalytic process, as confirmed by the PXRD patterns (Supplementary Fig. 40), and ICP-MS measurement of the solution after catalysis showed negligible leaching of the metal centres (2% for Ir, 0.1% for Ru, 0.5% for Pt, and no leaching for Zr and Hf). The catalytic activity (v) based on H_2 in the LP–HER-WOR-MOF over 72 h was 836 μmol g^{-1}. An apparent quantum yield of (1.5 ± 1)% at 436 nm was obtained by counting the number of absorbed photons and the number of generated H_2 and O_2 molecules during the catalysis (Supplementary Table 6, Supplementary Figs. 41 and 42)[41–44]. The H_2-TOF was 3.1 h^{-1} (a TON of 223 over 72 h) based on Pt, whereas the O_2-TOF was 0.19 h^{-1} (a TON of 14 over 72 h) based on Ir (where the Pt/Ir ratio was 0.1 in the sample). We noted that the amounts of redox relays (Fe^{3+} and TCBQ) were only two or three equivalents with respect to the Ir centres. As the generation of one O_2 molecule requires four equivalents of the one-electron oxidants, the observed H_2 and O_2 evolution must come from the overall water splitting instead of sacrificial reactions. When D_2O was used in the experiment, D_2 was observed along with a small amount of HD, confirming the splitting of water to generate hydrogen. All components in the LP–HER-WOR-MOFs are therefore critical for overall water splitting. For example, removing the TCBQ or the Fe^{3+} redox shuttle in the system led to notably reduced H_2 and O_2 generation (Supplementary Table 7). The lipid bilayer is also crucial, as incorporating both the HER-MOF (without hydrophobic modification) and the WOR-MOF together during the hydration step into the hydrophilic interior of the liposome resulted in a significantly decreased overall water-splitting activity (Fig. 5d). The liposomal structure was intact during the first 36 h but began to degrade after that, as confirmed by both dye-releasing experiments (Supplementary Fig. 43) and confocal images of the liposomes (Supplementary Fig. 44). The water-splitting activity of the LP–HER-WOR-MOF also decreased after 36 h, possibly due to destruction of the liposomal structure. The degradation is possibly caused by generation of reactive oxygen species during the reaction.

Photochemical processes in the HER-MOF. Femtosecond and nanosecond transient absorption spectroscopies (fsTA: 100 fs to 3.5 ns with 410 nm excitation; nsTA: 5 ns to 3.3 ms with 532 nm excitation) were used to obtain further insight into the photocatalytic process (Fig. 6). Global fitting of the fsTA spectrum of Hf-[(TCPP)Zn]-MOF gave five time constants, of ~100 fs, 1.6 ps, 26 ps, ~100 ps and 1.0 ns, together with a long-lasting component for the triplet excited state (Supplementary Figs. 45–49 and Supplementary Table 8). The time for intersystem crossing was 1.0 ns, which is consistent with the fluorescence lifetime (Supplementary Fig. 50 and Supplementary Table 9). The first three time constants are due to S_2–S_1 internal conversion (from the Soret band to the Q band) and

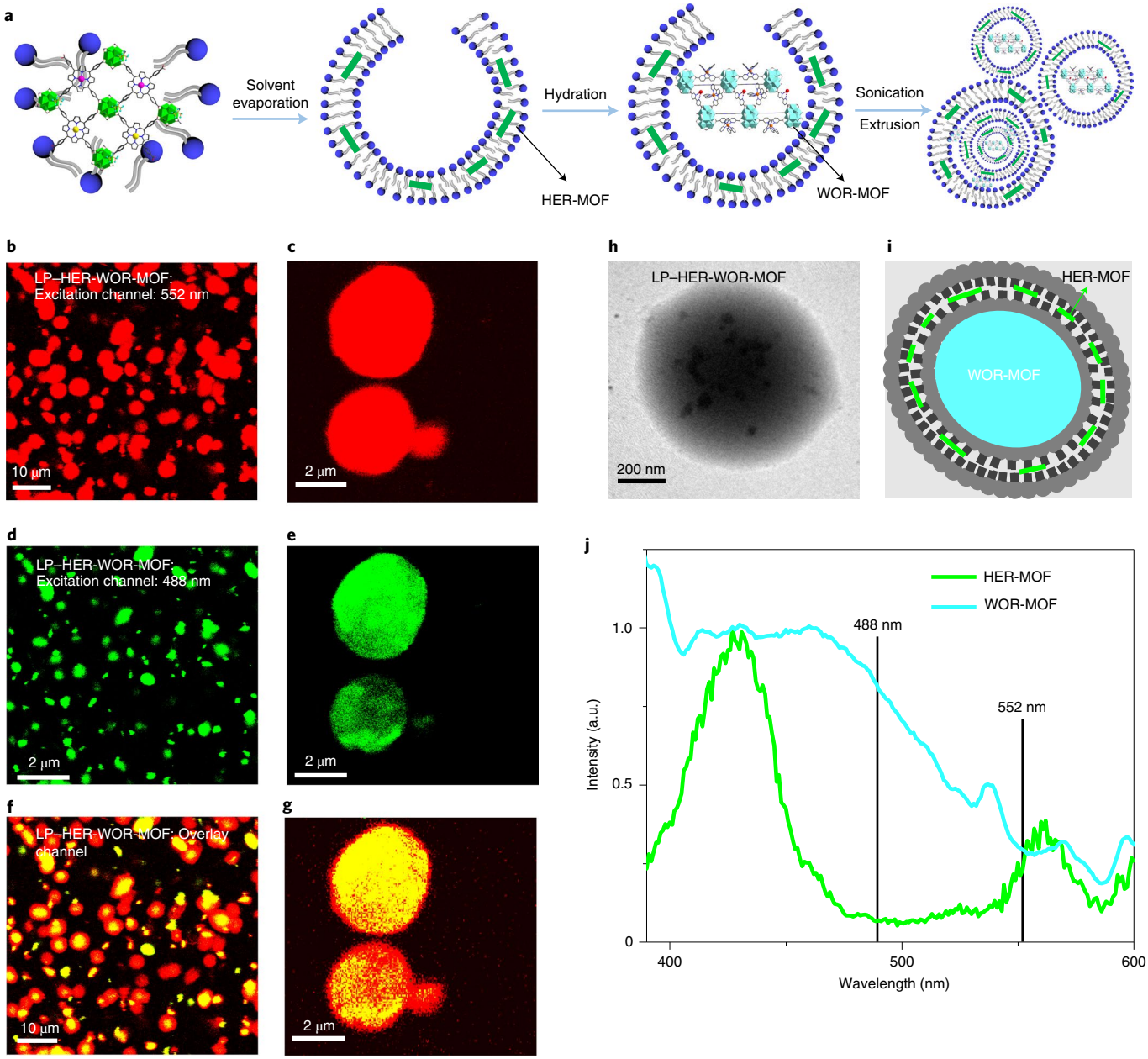

Fig. 4 | Construction and confocal fluorescence microscopy images of LP–HER-WOR-MOF. a, Assembling the hydrophobically modified HER-MOF with lecithin/cholesterol/TCBQ gave a bilayer film on a glass surface after solvent removal, which was hydrated and sonicated to form vesicles that wrap a fraction of WOR-MOF and Fe^{3+} in the aqueous phase; the mixture was then pushed through an extruder (1 μm) to reshape large liposomes and remove most of the unwrapped WOR-MOFs that aggregated into particles larger than the pore size. **b**,**d**,**f**, Confocal fluorescence microscopy images of LP–HER-WOR-MOF at different excitation wavelengths. Emissions were collected in the wavelength range of 600–700 nm: red represents HER-MOF + WOR-MOF and green represents WOR-MOF, whereas overlay of green and red gives a yellow colour to represent the overlap of the two MOFs. There is a thin shell of the liposome containing HER-MOF but not WOR-MOF, consistent with distribution of HER-MOF in the bilayer and WOR-MOF in the inner cavity. **c**,**e**,**g**, Higher resolution confocal images of the LP–HER-WOR-MOF at different excitation wavelengths. **h**, TEM image of the LP–HER-WOR-MOF showing WOR-MOF as small dark dots inside the liposome. **i**, Schematic of the LP–HER-WOR-MOF showing HER-MOF as green blocks within the lipid bilayer and marking the space containing WOR-MOF as the blue area. **j**, Excitation spectra of HER-MOF and WOR-MOF.

intramolecular vibrational relaxation[45]. The formation of the S_1 state is represented by a stimulated emission (SE) band at around 665 nm in the evolution associated difference spectra (Supplementary Fig. 49b and Fig. 6a) of a homogeneous control sample. The S_1 state in the Hf-[(TCPP)Zn]-MOF split into two singlet excitonic states, S_{1h} (higher energy at 650 nm) and S_{1l} (lower energy at 675 nm), due to electronic coupling between adjacent [(TCPP)Zn] moieties (Fig. 6a). The two states equilibrate at a time of ~100 ps (Supplementary Fig. 49d). The SE signal of the HER-MOF with both [(TCPP)Zn] and [(TCPP)Pt] shifted to 655 nm, which is absent in either Hf-[(TCPP)Zn]-MOF or Hf-[(TCPP)Pt]-MOF, indicating a new excitonic state S_{1mix} from electronic coupling between [(TCPP)Zn] and [(TCPP)Pt] (Fig. 6a and Supplementary Fig. 49d), which is also confirmed by fluorescence spectroscopy (Supplementary Figs. 50–52). Importantly, the addition of phenol to the HER-MOF suspension neither changed the fsTA results (Supplementary

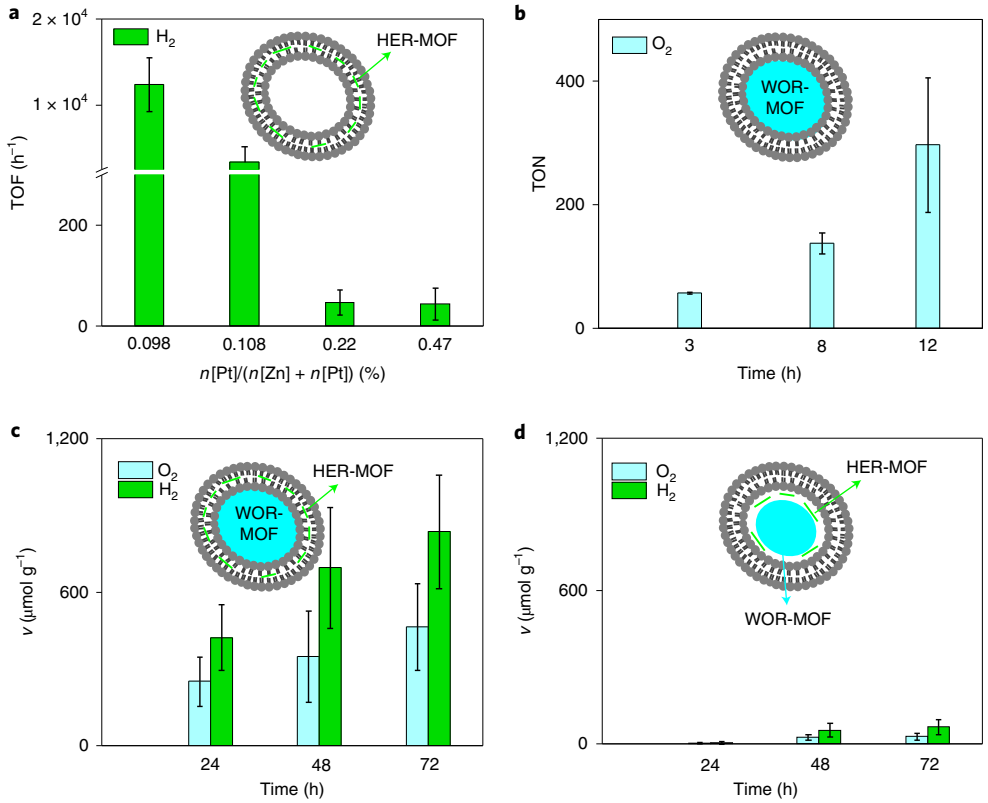

Fig. 5 | Photocatalytic activity of LP-MOF hybrids. a, Photocatalytic hydrogen evolution by the LP-HER-MOF with different [(TCPP)Pt] doping levels under visible-light irradiation (light source: 400 nm LED) showing higher TOFs at lower [(TCPP)Pt] doping levels due to concentrated photo-produced electrons at individual [(TCPP)Pt] centres in the antennae providing multi-electron injection for the HER. **b**, Photocatalytic water oxidation by the LP-WOR-MOF under visible-light irradiation (light source: 450 nm LED) showing progressive O_2 evolution. TON, turnover number. **c**, Overall water splitting by the LP-HER-WOR-MOF under visible-light irradiation (light source: 400 nm LED + 450 nm LED) showing H_2 and O_2 produced in a roughly 2:1 ratio. **d**, Overall water splitting by the unmodified hydrophilic HER-MOF and WOR-MOF inside the liposome to be compared with the LP-HER-WOR-MOF shown in **c**, demonstrating the importance of separation of the HER- and WOR-MOFs by the liposomal structure for overall water splitting. The error bars represent ± the standard deviation obtained from three independent tests.

Figs. 47 and 49) nor quenched the fluorescence (Supplementary Figs. 53 and 54), suggesting that electron transfer happens over a longer time scale.

The triplet excited states were then monitored by nsTA spectroscopy at 490 nm, which is the maximum of the excited state absorption. However, phenol does not quench triplet excited states in either the Hf-[(TCPP)Zn]-MOF (lifetime: 52.6 μs) or the homogeneous solution of [(TCPP)Zn] (58 μs) (Supplementary Figs. 55 and 56 and Supplementary Table 10)[46]. On the other hand, doping [(TCPP)Pt] into the MOF shortened the lifetime to 1.5 μs in HER-MOF, possibly due to dissociation of the excitonic state (T_{1mix} from intersystem crossing of S_{1mix}) to generate $[(TCPP)Pt]^-$ and $[(TCPP)Zn]^+$ (Fig. 6b). A residual component representing $[(TCPP)Zn]^+$ finally decayed with a time constant of 0.32 ms, which corresponds to the rate of charge recombination. The addition of 0.15 mM of phenol significantly shortened this time to 0.19 ms, indicating a reaction between phenol and $[(TCPP)Zn]^+$ to regenerate [(TCPP)Zn] (Fig. 6c).

The HER thus occurs via light-induced charge separation between [(TCPP)Zn] and [(TCPP)Pt]. The generated $[(TCPP)Pt]^-$ is then protonated to [(TCPP)Pt-H], which accepts another electron and another proton to release one H_2 molecule (Fig. 7a).

Photochemical processes in the WOR-MOF. For the WOR side, global fitting of the fsTA spectra of Zr-$[Ru]^{2+}$-MOF gave two fast components with time constants of 660 fs and 4.2 ps that are due to fast intramolecular vibrational relaxation and triplet metal-to-ligand charge transfer (^{3}MLCT) dynamics involving inter-ligand electron transfer (Supplementary Figs. 57–59, Supplementary Table 11)[47]. There is also a long-lasting component (lifetime > 10 ns) assigned as the relaxed ^{3}MLCT state of $[Ru]^{2+*}$ (ref. [47]). In the WOR-MOF, excited-state dynamics of the [(BPYDC)Ir] reaction centre were also observed with a time constant of 79 ps. The $[Ru]^{2+*}$ excited state was quenched with a time constant of 1.9 ns, possibly through energy transfer. The addition of Fe^{3+} (37 mM) to the suspension of the WOR-MOF gave a significant change even within the first 660 fs. The decay-associated difference spectra of the initial component indicated a fast build-up of negative signals in the 500–600 nm region (Fig. 6d and Supplementary Figs. 60 and 61), which is consistent with the generation of $[Ru]^{3+}$ from $[Ru]^{2+*}$ (ref. [47]) ($[Ru]^{3+}/[Ru]^{2+*}$ 0.35 V_{NHE} versus Fe^{3+}/Fe^{2+} 0.77 V_{NHE}). This fast electron transfer is also consistent with static phosphorescence quenching of $[Ru]^{2+*}$ by Fe^{3+} (Fig. 6d,e). The decay-associated difference spectra of this component are also similar to that of the photo-oxidation of $[Ru]^{2+}$ using $Na_2S_2O_8$ (42 mM) (Fig. 6f and Supplementary Fig. 54). The $[Ru]^{3+}$ then oxidizes Ir to a higher oxidation state ($[Ru]^{3+}/[Ru]^{2+}$ 1.47 V_{NHE} versus $[(BPYDC)Ir]/[(BPYDC)Ir]^+$ 1.34 V_{NHE})[29,40], possibly with a time constant of 0.92 ns (Supplementary Table 11).

The WOR is thus initiated by the photo-oxidation of $[Ru]^{2+*}$ by Fe^{3+} to produce $[Ru]^{3+}$, which in turn oxidizes [(BPYDC)Ir] for water oxidation (Fig. 7b and Supplementary Table 12)[48–50].

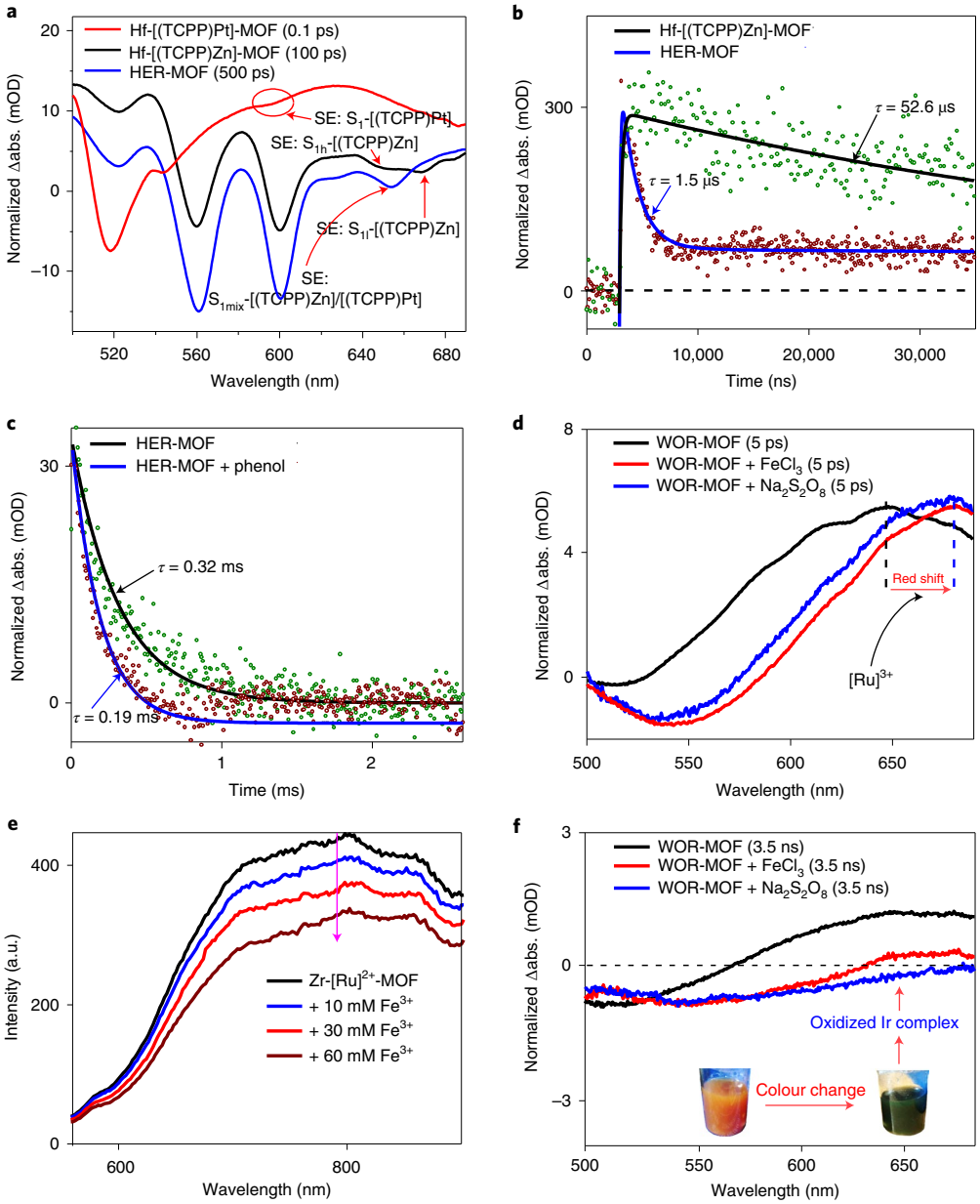

Fig. 6 | Transient absorption spectra of HER-MOF and WOR-MOF. a, The fsTA spectra of the Hf-[(TCPP)Zn]-MOF, HER-MOF and Hf-[(TCPP)Pt]-MOF, showing the emergence of an excitonic state. **b**, Time trace nsTA spectra at 490 nm of Hf-[(TCPP)Zn]-MOF and HER-MOF, showing the decay signal of the triplet excited state of [(TCPP)Zn] with a lifetime of 52.6 ± 0.7 μs using a mono-exponential model [$y = A\exp(-t/\tau)$, where $A = 37.2 \pm 0.2$ and $\tau = 52.6 \pm 0.7$ μs], and formation of charge-separated $[(TCPP)Pt]^-$ and $[(TCPP)Zn]^+$ species in the HER-MOF with a time constant of 1.5 ± 0.1 μs using a bi-exponential model [$y = A_1(\exp -t/\tau_1) + A_2\exp(-t/\tau_2)$, where $A_1 = 272 \pm 1$, $\tau_1 = 1.5 \pm 0.1$ μs, $A_2 = 62.8 \pm 0.2$ and $\tau_2 = 47 \pm 4$ μs]. **c**, Time trace nsTA spectra at 490 nm of the HER-MOF and HER-MOF + 0.015 mM phenol, showing recombination of $[(TCPP)Pt]^-$ and $[(TCPP)Zn]^+$ in the HER-MOF with a time constant of 0.32 ± 0.01 ms using a mono-exponential model [$y = A\exp(-t/\tau)$, where $A = 32.7 \pm 0.1$ and $\tau = 0.32 \pm 0.01$ ms] and phenol to quench the generated $[(TCPP)Zn]^+$ with a reduced time constant of 0.19 ± 0.005 ms using a mono-exponential model [$y = A\exp(-t/\tau)$, where $A = 34.6 \pm 0.1$ and $\tau = 0.19 \pm 0.005$ ms]. The errors of the fitted time constants in **b** and **c** are the standard deviations obtained from data fitting. **d**, The fsTA spectra of the WOR-MOF, WOR-MOF + $FeCl_3$ and WOR-MOF + $Na_2S_2O_8$ at 5 ps, showing fast electron transfer to produce Ru^{3+} by a red shift of the spectra. **e**, Quenching of the $[Ru]^{2+}$ emission by different concentrations of Fe^{3+}, confirming electron transfer between the two. **f**, The fs TA spectra of the WOR-MOF, WOR-MOF + $FeCl_3$ and WOR-MOF + $Na_2S_2O_8$ at 3.5 ns, suggesting the generation of high-valence Ir species on this time scale in the presence of oxidant, which is consistent with the colour change of the WOR-MOF + $Na_2S_2O_8$ after irradiation.

Charge recombination. The lipid bilayer prevents direct charge recombination between the HER-MOF and the WOR-MOF. Furthermore, TCBQ/TCBQH added to the lipid bilayer is not in contact with the WOR-MOF, which is consistent with the lack of phosphorescence quenching of the Zr-$[Ru]^{2+}$-MOF by TCBQ in the liposomal assembly (Supplementary Fig. 61) and avoids reaction between TCBQH and oxidative species in the WOR-MOF. Similarly, the Fe^{3+}/Fe^{2+} pair added in the hydration step in the aqueous phase is not in contact with the HER-MOF, as evidenced by the lack of fluorescence quenching of the Hf-[(TCPP)Zn]-MOF by Fe^{3+} in the assembly (Supplementary Fig. 30). On the other hand, a redox reaction between Fe^{3+}/Fe^{2+} (0.77 V_{NHE}) and TCBQ/TCBQH

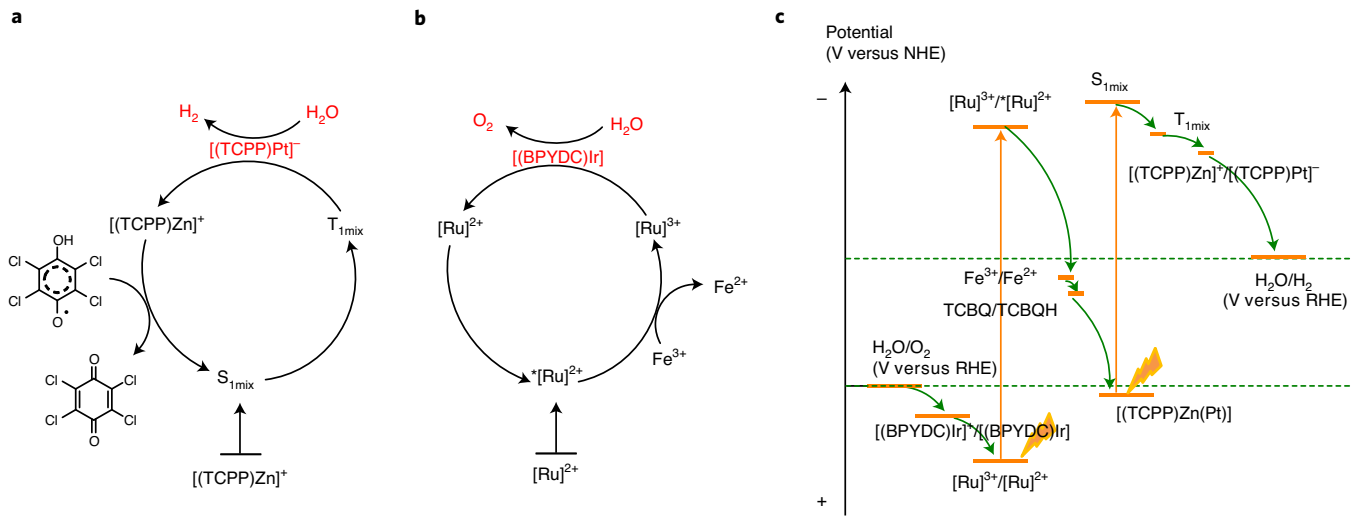

Fig. 7 | The photocatalytic cycle and energy level diagram. a, Photocatalytic hydrogen evolution cycle. **b**, Photocatalytic water oxidation cycle. **c**, Energy level diagram of overall water splitting. The energy levels are either determined by electrochemical/photophysical measurements or estimated based on values in the literature. To sum up, photo-excitation of $[Ru]^{2+}$ in the WOR-MOF initiates its oxidation by Fe^{3+} to produce high-valence Ir species that oxidize water to O_2 and generate a proton. Fe^{2+} and the proton react with TCBQ at the lipid/water interface to produce reduced TCBQH and Fe^{3+}. In the HER-MOF, [(TCPP)Zn]/[(TCPP)Pt] are excited to an excitonic triplet state that undergoes charge separation to produce $[(TCPP)Pt]^-$ and $[(TCPP)Zn]^+$. TCBQH is oxidized by $[(TCPP)Zn]^+$ and releases a proton to $[(TCPP)Pt]^-$ and thus [(TCPP)Pt-H] is obtained, which accepts another electron and proton to release H_2.

($0.8\,V_{NHE}$) can happen efficiently at the interface of the liposome (Supplementary Fig. 62a). This is facilitated by favourable adsorption of Fe^{3+}/Fe^{2+} on the polar heads of the lipid (Supplementary Fig. 62b). Charge recombination can still occur between TCBQ and the reductive species in the HER-MOF or Fe^{2+} and the oxidative species in the WOR-MOF. The latter process is considered as the major recombination channel, as Fe^{2+} is detected in the aqueous solution by UV-visible spectroscopy using phenanthroline as an indicator of photocatalysis, while the resting state of TCBQ in the reaction is in its reductive form as confirmed by the lack of fluorescence quenching of [(TCPP)Zn] (Supplementary Fig. 63). The accumulated Fe^{2+} in the water-splitting process indicated unbalanced reaction rates in the HER and WOR sides, that is, the overall rate of the HER (reduction side) is slower than the WOR (oxidation side), so redox shuttles are trapped in their reductive form that can recombine with oxidative species like $[Ru(BPY)_3]^{3+}$, limiting the quantum efficiency in the current system.

The overall water-splitting process. The overall water splitting process is thus initiated by the photo-oxidation of $[Ru]^{2+}$ in the WOR-MOF by Fe^{3+}, followed by hole transfer to Ir^{III} centres to generate $Ir^{IV/V}$ species, which oxidize water to O_2 with concomitant generation of a proton. The generated Fe^{2+} is then adsorbed to the lipid/water interface where it reacts with TCBQ to afford the reduced TCBQH and Fe^{3+}. The proton on the TCBQH comes from water. Another photon excites the [(TCPP)Zn]/[(TCPP)Pt] to an excitonic triplet state in the HER-MOF, which undergoes charge separation to generate $[(TCPP)Pt]^-$ and $[(TCPP)Zn]^+$. The $[(TCPP)Zn]^+$ oxidizes the TCBQH back to TCBQ and releases the proton; the $[(TCPP)Pt]^-$ is protonated to [(TCPP)Pt-H], which accepts another electron and proton to release H_2 to complete the overall water-splitting cycle (Fig. 7c and Supplementary Figs. 64–67 and Supplementary Table 12).

Conclusion

We show evidence for overall photocatalytic water splitting by hierarchically assembling a HER-MOF, constructed from hydrophobically modified $Hf_6(\mu_3\text{-}O)_4(\mu_3\text{-}OH)_4$ clusters with pentafluoropropionate groups and [(TCPP)Zn]/[(TCPP)Pt] linkers, and a WOR-MOF, constructed from $Zr_{12}(\mu_3\text{-}O)_8(\mu_3\text{-}OH)_8(\mu_2\text{-}OH)_6$ clusters and $[Ru]^{2+}$ and [(BPYDC)Ir] linkers, in liposome vesicles. Connected by the Fe^{3+}/Fe^{2+} and TCBQ/TCBQH redox relays, these MOFs use sunlight energy (irradiation) to convert water into chemical fuels (H_2 and O_2) through the 'Z-scheme'. The lipid membrane separates the oxidative and reductive components of the system to avoid charge recombination. Transient absorption spectroscopy studies confirmed fast electron transport from the antennae to the reaction centres in this artificial photosynthetic system. The efficiency of the current hybrid system is limited, with an apparent quantum yield of $(1.5 \pm 1)\%$, by unbalanced rates of the HER and WOR sides in which a slower overall rate of the HER compared with the WOR gives rise to the accumulation of redox shuttles in the reductive form that can recombine with oxidative species like $[Ru(BPY)_3]^{3+}$ on the oxidation side. This, we hope can be improved in future studies. Importantly, this work highlights the hierarchical organization of MOF components into biomimetic hybrid assemblies to accomplish complex functions.

Online content

Any methods, additional references, Nature Research reporting summaries, source data, extended data, supplementary information, acknowledgements, peer review information; details of author contributions and competing interests; and statements of data and code availability are available at https://doi.org/10.1038/s41557-020-00635-5.

Received: 13 May 2019; Accepted: 18 December 2020;
Published online: 15 February 2021

References

1. Ciamician, G. The photochemistry of the future. *Science* **36**, 385–394 (1912).
2. Barber, J. Photosynthetic energy conversion: natural and artificial. *Chem. Soc. Rev.* **38**, 185–196 (2009).

3. Favereau, L. et al. A molecular tetrad that generates a high-energy charge-separated state by mimicking the photosynthetic Z-scheme. *J. Am. Chem. Soc.* **138**, 3752–3760 (2016).
4. Kothe, T. et al. Combination of a photosystem 1-based photocathode and a photosystem 2-based photoanode to a Z-scheme mimic for biophotovoltaic applications. *Angew. Chem. Int. Ed.* **52**, 14233–14236 (2013).
5. Tian, H., Yu, Z., Hagfeldt, A., Kloo, L. & Sun, L. Organic redox couples and organic counter electrode for efficient organic dye-sensitized solar cells. *J. Am. Chem. Soc.* **133**, 9413–9422 (2011).
6. Sokol, K. P. et al. Bias-free photoelectrochemical water splitting with photosystem II on a dye-sensitized photoanode wired to hydrogenase. *Nat. Energy* **3**, 944–951 (2018).
7. Li, Z. et al. Biomimetic electron transport via multiredox shuttles from photosystem II to a photoelectrochemical cell for solar water splitting. *Energy Environ. Sci.* **10**, 765–771 (2017).
8. Tachibana, Y., Vayssieres, L. & Durrant, J. R. Artificial photosynthesis for solar water-splitting. *Nat. Photonics* **6**, 511–518 (2012).
9. Li, F. et al. Organic dye-sensitized tandem photoelectrochemical cell for light driven total water splitting. *J. Am. Chem. Soc.* **137**, 9153–9159 (2015).
10. Gurudayal et al. Perovskite–hematite tandem cells for efficient overall solar driven water splitting. *Nano Lett.* **15**, 3833–3839 (2015).
11. Wang, W., Li, Z., Chen, J. & Li, C. Crucial roles of electron–proton transport relay in the photosystem II-photocatalytic hybrid system for overall water splitting. *J. Phys. Chem. C* **121**, 2605–2612 (2017).
12. Cui, Y. et al. Metal–organic frameworks as platforms for functional materials. *Acc. Chem. Res.* **49**, 483–493 (2016).
13. Fateeva, A. et al. A water-stable porphyrin-based metal–organic framework active for visible-light photocatalysis. *Angew. Chem. Int. Ed.* **51**, 7440–7444 (2012).
14. Kalmutzki, M. J., Hanikel, N. & Yaghi, O. M. Secondary building units as the turning point in the development of the reticular chemistry of MOFs. *Sci. Adv.* **4**, eaat9180 (2018).
15. Maza, W. A., Padilla, R. & Morris, A. J. Concentration dependent dimensionality of resonance energy transfer in a postsynthetically doped morphologically homologous analogue of UiO-67 MOF with a ruthenium(II) polypyridyl complex. *J. Am. Chem. Soc.* **137**, 8161–8168 (2015).
16. Son, H. J. et al. Light-harvesting and ultrafast energy migration in porphyrin-based metal–organic frameworks. *J. Am. Chem. Soc.* **135**, 862–869 (2013).
17. Choi, K. M. et al. Plasmon-enhanced photocatalytic CO_2 conversion within metal–organic frameworks under visible light. *J. Am. Chem. Soc.* **139**, 356–362 (2017).
18. Nilsson, T. et al. Lipid-mediated protein-protein interactions modulate respiration-driven ATP synthesis. *Sci. Rep.* **6**, 24113 (2016).
19. Steinberg-Yfrach, G. et al. Conversion of light energy to proton potential in liposomes by artificial photosynthetic reaction centres. *Nature* **385**, 239–241 (1997).
20. Li, Y. et al. Supramolecular assembly of photosystem II and adenosine triphosphate synthase in artificially designed honeycomb multilayers for photophosphorylation. *ACS Nano.* **12**, 1455–1461 (2018).
21. Limburg, B. et al. Kinetics of photocatalytic water oxidation at liposomes: membrane anchoring stabilizes the photosensitizer. *ACS Catal.* **6**, 5968–5977 (2016).
22. Limburg, B., Bouwman, E. & Bonnet, S. Molecular water oxidation catalysts based on transition metals and their decomposition pathways. *Coord. Chem. Rev.* **256**, 1451–1467 (2012).
23. Fang, X. et al. Single Pt atoms confined into a metal–organic framework for efficient photocatalysis. *Adv. Mater.* **30**, 1705112 (2018).
24. Wang, C., Wang, J.-L. & Lin, W. Elucidating molecular iridium water oxidation catalysts using metal–organic frameworks: a comprehensive structural, catalytic, spectroscopic, and kinetic study. *J. Am. Chem. Soc.* **134**, 19895–19908 (2012).
25. Hu, Z. et al. Kinetically controlled synthesis of two-dimensional Zr/Hf metal–organic framework nanosheets via a modulated hydrothermal approach. *J. Mater. Chem. A* **5**, 8954–8963 (2017).
26. Maza, W. A. & Morris, A. J. Photophysical characterization of a ruthenium(II) tris(2,2′-bipyridine)-doped zirconium UiO-67 metal–organic framework. *J. Phys. Chem. C* **118**, 8803–8817 (2014).
27. Feng, D. et al. Zirconium-metalloporphyrin PCN-222: mesoporous metal–organic frameworks with ultrahigh stability as biomimetic catalysts. *Angew. Chem. Int. Ed.* **51**, 10307–10310 (2012).
28. He, T. et al. Ultrathin 2D zirconium metal–organic framework nanosheets: preparation and application in photocatalysis. *Small* **14**, 1703929 (2018).
29. Dai, R. et al. Electron crystallography reveals atomic structures of metal–organic nanoplates with $M_{12}(\mu_3\text{-}O)_8(\mu_3\text{-}OH)_8(\mu_2\text{-}OH)_6$ (M = Zr, Hf) secondary building units. *Inorg. Chem.* **56**, 8128–8134 (2017).
30. Cliffe, M. J. et al. Metal–organic nanosheets formed via defect-mediated transformation of a hafnium metal–organic framework. *J. Am. Chem. Soc.* **139**, 5397–5404 (2017).
31. Xie, R., Hong, S., Feng, L., Rong, J. & Chen, X. Cell-selective metabolic glycan labeling based on ligand-targeted liposomes. *J. Am. Chem. Soc.* **134**, 9914–9917 (2012).
32. Wang, C., deKrafft, K. E. & Lin, W. Pt nanoparticles@photoactive metal–organic frameworks: efficient hydrogen evolution via synergistic photo-excitation and electron injection. *J. Am. Chem. Soc.* **134**, 7211–7214 (2012).
33. Lv, H. et al. A noble-metal-free, tetra-nickel polyoxotungstate catalyst for efficient photocatalytic hydrogen evolution. *J. Am. Chem. Soc.* **136**, 14015–14018 (2014).
34. Kim, D., Whang, D. R. & Park, S. Y. Self-healing of molecular catalyst and photosensitizer on metal–organic framework: robust molecular system for photocatalytic H_2 evolution from water. *J. Am. Chem. Soc.* **138**, 8698–8701 (2016).
35. Zhang, F.-M. et al. Rational design of MOF/COF hybrid materials for photocatalytic H_2 evolution in the presence of sacrificial electron donors. *Angew. Chem. Int. Ed.* **57**, 12106–12110 (2018).
36. Eckenhoff, W. T. & Eisenberg, R. Molecular systems for light driven hydrogen production. *Dalton Trans.* **41**, 13004–13021 (2012).
37. Bae, E. & Choi, W. Effect of the anchoring group (carboxylate vs phosphonate) in Ru-complex-sensitized TiO_2 on hydrogen production under visible light. *J. Phys. Chem. B* **110**, 14792–14799 (2006).
38. Lan, Q. et al. Highly dispersed polyoxometalate-doped porous Co_3O_4 water oxidation photocatalysts derived from POM@MOF crystalline materials. *Chem. Eur. J.* **22**, 15513–15520 (2016).
39. Huang, Z. et al. Efficient light-driven carbon-free cobalt-based molecular catalyst for water oxidation. *J. Am. Chem. Soc.* **133**, 2068–2071 (2011).
40. Chi, L., Xu, Q., Liang, X., Wang, J. & Su, X. Iron-based metal–organic frameworks as catalysts for visible light-driven water oxidation. *Small* **12**, 1351–1358 (2016).
41. Wang, Q. et al. Particulate photocatalyst sheets based on carbon conductor layer for efficient Z-scheme pure-water splitting at ambient pressure. *J. Am. Chem. Soc.* **139**, 1675–1683 (2017).
42. Iwase, A., Ng, Y. H., Ishiguro, Y., Kudo, A. & Amal, R. Reduced graphene oxide as a solid-state electron mediator in Z-scheme photocatalytic water splitting under visible light. *J. Am. Chem. Soc.* **133**, 11054–11057 (2011).
43. Melo, M. A. et al. Surface photovoltage measurements on a particle tandem photocatalyst for overall water splitting. *Nano Lett.* **18**, 805–810 (2018).
44. Zhu, M., Sun, Z., Fujitsuka, M. & Majima, T. Z-scheme photocatalytic water splitting on a 2D heterostructure of black phosphorus/bismuth vanadate using visible light. *Angew. Chem. Int. Ed.* **57**, 2160–2164 (2018).
45. Gurzadyan, G. G., Tran-Thi, T.-H. & Gustavsson, T. Time-resolved fluorescence spectroscopy of high-lying electronic states of Zn-tetraphenylporphyrin. *J. Chem. Phys.* **108**, 385–388 (1998).
46. Tran Thi, T. H., Desforge, C., Thiec, C. & Gaspard, S. Singlet–singlet and triplet–triplet intramolecular transfer processes in a covalently linked porphyrin–phthalocyanine heterodimer. *J. Phys. Chem.* **93**, 1226–1233 (1989).
47. Reichardt, C. et al. Excited state dynamics of a photobiologically active Ru(II) dyad are altered in biologically relevant environments. *J. Phys. Chem. A* **121**, 5635–5644 (2017).
48. Limburg, B., Bouwman, E. & Bonnet, S. Rate and stability of photocatalytic water oxidation using $[Ru(bpy)_3]^{2+}$ as photosensitizer. *ACS Catal.* **6**, 5273–5284 (2016).
49. Wang, C., Xie, Z., deKrafft, K. E. & Lin, W. Light-harvesting cross-linked polymers for efficient heterogeneous photocatalysis. *ACS Appl. Mater. Interfaces* **4**, 2288–2294 (2012).
50. Hong, D., Yamada, Y., Nagatomi, T., Takai, Y. & Fukuzumi, S. Catalysis of nickel ferrite for photocatalytic water oxidation using $[Ru(bpy)_3]^{2+}$ and $S_2O_8^{2-}$. *J. Am. Chem. Soc.* **134**, 19572–19575 (2012).

Methods

Catalyst preparation. *Synthesis of the Hf-[(TCPP)Zn(Pt)]-MOF (HER-MOF).* The synthetic procedure for the Hf-[(TCPP)Zn(Pt)]-MOF was modified from that of a previously reported MOF[28]. However, the resultant MOF structure is different from the reported one. A mixture of $HfCl_4$ (19.2 mg, 60 μmol) and [(H_4TCPP)Zn] (8.6 mg, 10 μmol) was dissolved in a mixture of DMF (1.6 ml), HCO_2H (0.75 ml) and H_2O (0.66 ml) in a Pyrex vial, and was kept at 120 °C for three days. The Hf-[(TCPP)Zn]-MOF was isolated as a powder by centrifugation before washing with DMF and H_2O several times (~90% yield). The Hf-[(TCPP)Zn(Pt)]-MOF series with mixed [(TCPP)Pt]/[(TCPP)Zn] ratios was synthesized following a similar procedure but with different [(TCPP)Pt]/[(TCPP)Zn] ratios. The resultant MOFs were then sonicated and filtered through a porous membrane (pore size 1 μm) to remove large pieces (~32% yield).

Determining the structure of the Hf-[(TCPP)Zn]-MOF. We assigned the structure of the Hf-[(TCPP)Zn]-MOF as Hf_6 SBUs linked by [(TCPP)Zn] ligands in an sql lattice (Supplementary Figs. 5 and 6). The evidence below supports this structure assignment.

First, HRTEM images of the Hf-[(TCPP)Zn]-MOF gave clear lattice patterns (Supplementary Fig. 7b) and the selected area electron diffraction image along the [001] zone axis (Supplementary Fig. 7b) can be indexed to (*hk*0) using a unit cell of dimensions $a = 39.76$ Å, $b = 16.65$ Å, $c = 43.11$ Å, $\alpha = 90°$, $\beta = 84°$ and $\gamma = 90°$ (the value of c and the accurate values of a and b were obtained from PXRD patterns). The STEM-HAADF image showed the arrangement of SBUs in a 4,4-connected sql topology with each SBU represented as a white dot (Supplementary Fig. 7c). The measured inter-SBU distances in the HAADF image were 1.69 nm in one direction (1.67 nm in the model, with 1% deviation) and 1.95 nm in the other direction (1.97 nm in the model, with 1% deviation), matching that of a zig-zag monolayer model of the Hf-[(TCPP)Zn]-MOF (Supplementary Fig. 5). HRTEM and electron diffraction of other regions of the sample gave another sql lattice with inter-SBU distances of 1.7 nm in one direction and 2.2 nm in the other direction (Supplementary Fig. 7d). These distances correspond to the structure of a flat lattice (Supplementary Fig. 6).

Second, AFM measurement of the Hf-[(TCPP)Zn]-MOF showed a thickness range of 1.3–2.2 nm (Supplementary Fig. 11). The 1.3 nm thickness matches roughly the height of the flat lattice while the 2.2 nm thickness matches roughly the height of the zig-zag lattice.

Third, the PXRD pattern was consistent with a combination of the simulated patterns of monolayers[31] of the flat and the zig-zag lattices (Supplementary Fig. 8).

Fourth, thermogravimetric analysis (TGA) gave a weight loss of 25% from room temperature to 350 °C (Supplementary Fig. 9), which corresponds to the loss of solvent and coordinated H_2O and formates; the 28% weight loss in the 350–465 °C range corresponds to the decomposition of [(TCPP)Zn], and the residual weight of 47% is due to HfO_2 and ZnO. The [(TCPP)Zn]/Hf ratio calculated from TGA is only slightly lower than 1:6, which is predicted from the structural models.

Fifth, the ^{1}H NMR spectrum of the dissolved Hf-[(TCPP)Zn]-MOF in d_6-dimethyl sulfoxide/K_3PO_4–D_2O (4:1) gave an $n(HCO_2H):n([(TCPP)Zn])$ ratio of 3.4:1 from the integrations (Supplementary Fig. 10). The formates coordinate to the sites on the SBUs that are not occupied by the carboxylates from the [(TCPP)Zn] ligands. The theoretical ratio of $n(HCO_2H):n([(TCPP)Zn])$ was 3:1 for the Hf_6-[(TCPP)Zn]-MOF, which is close to the experimental value.

Sixth, the connections in the zig-zag and flat layers are chemically equivalent. Therefore, there is no energy preference for forming one structure over the other. The real structure can be a combination of the two, even within one nanosheet.

Hydrophobic modification of the HER-MOF. The Hf-[(TCPP)Zn(Pt)]-MOF was hydrophobically modified by replacing the capping formates with pentafluoropropionate groups. The MOF was dispersed in DMF and reacted with three equivalents of pentafluoropropionic acid in the solution at 60 °C for 6 h before being washed with DMF and ethanol multiple times. The contact angle of the resultant HER-MOF was measured by drop-drying the MOF on a clean silicon wafer to form a film for the test.

Synthesis and characterization of the Zr-[Ru]$^{2+}$-MOF. The Zr-[Ru]$^{2+}$-MOF was synthesized following procedure similar to that for a previously reported MOF[29]. A mixture of $ZrCl_4$ (20 mg, 86 μmol), H_2BPYDC (20 mg, 82 μmol) and [Ru]$^{2+}$ (11.7 mg, 16 μmol) was dissolved in a mixture of DMF (3.6 ml), HCO_2H (1.0 ml) and H_2O (4.4 ml) in a Pyrex vial, and was kept at 120 °C for two days. The Zr-[Ru]$^{2+}$-MOF was isolated as a powder by centrifugation before being washed with DMF and H_2O multiple times, and was obtained in 80% yield. The phase purity of the synthesized MOF was supported by the similarity between the experimental and simulated PXRD patterns (Supplementary Fig. 17).

Synthesis of the WOR-MOF. The WOR-MOF was prepared by coordinating $IrCl_3{\cdot}3H_2O$ or $Ir(NO_3)_3$ onto the Zr-[Ru]$^{2+}$-MOF. The $Ir(NO_3)_3$ was prepared by heating $IrCl_3{\cdot}3H_2O$ (300 mg, 1.0 μmol), $AgNO_3$ (550 mg, 3.2 μmol) and H_2O (30 ml) in a 50 ml round-bottomed flask at 60 °C in the dark overnight before removing the AgCl precipitate by filtration through diatomaceous earth. The filtrate was used directly for reaction with Zr-[Ru]$^{2+}$-MOF (320 mg, 0.2 μmol) at 90 °C in the dark overnight. Loading of $IrCl_3{\cdot}3H_2O$ (108 mg, 0.34 μmol) was similarly achieved by reaction with Zr-[Ru]$^{2+}$-MOF (320 mg, 0.2 μmol) at 90 °C in the dark overnight. The resultant WOR-MOF was isolated through centifugation, then washed with H_2O and DMF multiple times. The phase purity of the WOR-MOF was supported by the similarity between the experimental and simulated PXRD patterns (Supplementary Fig. 17).

Synthesis of the LP–HER-MOF. The liposomes were synthesized following similar procedures in the literature using a film-dispersion method[31]. To a 100 ml round-bottomed flask was added PC (1.71 ml, 10 mg ml^{-1}), Chol (291 μl, 10 mg ml^{-1}) and the HER-MOF (1.71 mg). The solvent was removed by rotary evaporation to leave a thin film on the wall of the flask. The flask was kept in vacuo overnight. The dried lipid film was then hydrated in the presence of Pyrex glass beads in the dark with aqueous solution. The mixture was ultra-sonicated for 10 min, followed by ten freeze–thaw cycles using liquid N_2, and then immersed in a 55 °C water bath to form a multilamellar vesicle suspension. The suspension was cooled slowly to room temperature over 30 min before being extruded with a mini-extruder (Avanti Polar Lipids) at room temperature using a polycarbonate membrane (pore size 1 μm) for 11 cycles to obtain the LP–HER-MOF.

Synthesis of the LP–WOR-MOF. To a 100 ml round-bottomed flask was added PC (1.71 ml, 10 mg ml^{-1}) and Chol (291 μl, 10 mg ml^{-1}). The solvent was removed by rotary evaporation to leave a thin film on the wall of the flask. The flask was kept in vacuo overnight. The dried lipid film was then hydrated in the presence of WOR-MOF (1.71 mg). The mixture was then ultra-sonicated for 10 min, followed by ten freeze–thaw cycles using liquid N_2, and then immersed in a 55 °C water bath to form a multilamellar vesicle suspension. The suspension was cooled slowly to room temperature over 30 min before being extruded with a mini-extruder at room temperature using a polycarbonate membrane (pore size 1 μm) for 11 cycles to obtain the LP–WOR-MOF.

Synthesis of the LP–HER-WOR-MOF. To a 100 ml round-bottomed flask was added PC (1.71 ml, 10 mg ml^{-1}), Chol (291 μl, 10 mg ml^{-1}), TCBQ (1 mg) and the HER-MOF (1.71 mg). The solvent was removed by rotary evaporation to leave a thin film on the wall of the flask. The flask was kept in vacuo overnight. The dried lipid film was then hydrated in the presence of the WOR-MOF (1.71 mg) and $FeCl_3$ (1.5 mg). The mixture was then ultra-sonicated for 10 min, followed by ten freeze–thaw cycles using liquid N_2, and then immersed in a 55 °C water bath to form a multilamellar vesicle suspension. The suspension was cooled slowly to room temperature over 30 min before being extruded with a mini-extruder at room temperature using a polycarbonate membrane (pore size 1 μm) for 11 cycles to obtain the aqueous suspension of the LP–HER-WOR-MOF. The suspension contained liposomes with 10 mg ml^{-1} of PC, 10 mg ml^{-1} of Chol and 0.07 mg ml^{-1} of the HER MOF in the LP–HER-MOF assembly, and 0.04 mg ml^{-1} of the WOR-MOF in the LP–WOR-MOF assembly (the amounts of MOFs were determined using ICP-MS).

Determining the amount of MOFs in the LP–MOF assembly. Unwrapped MOFs were all removed during the extrusion step in liposome preparation, as they aggregated to form large pieces. The MOFs encapsulated in the liposomes were released by adding DMF to the liposome suspension to destroy the liposome and dissolve the lipids. The MOFs were then obtained by centrifugation (speed 9,600 rpm, ~6,000 *g*, time 5 min). The amount of MOFs was quantified by digesting them for ICP-MS analysis and the incorporation yield was thus obtained by dividing the amount of incorporated MOFs by the amount of MOFs initially added to the suspension.

General procedure for ICP-MS experiments. For ICP-MS measurements, 2 mg of the MOF was added to a mixture of concentrated hydrochloric acid (1.5 ml), concentrated nitric acid (0.5 ml) and hydrogen peroxide (two drops) and was kept at 200 °C overnight. ICP-MS analysis was performed using a SCIEX ELAN ICP-DRC-qMS instrument (PerkinElmer) equipped with a concentric pneumatic nebulizer (Meinhard) and a cyclonic spray chamber. Samples were diluted in a 5% nitric acid matrix and analysed with a ^{159}Tb internal standard against a six-point standard curve over the range from 1 to 100 ppm. The correlation coefficient was >0.9997 for all analytes of interest.

ICP-MS measurement of the supernatant after catalysis. After reaction, we added ethanol to the liposome suspension to destroy the liposome and dissolve the lipids. The MOFs were then obtained by centrifugation (speed 9,600 rpm, ~6,000 *g*, time 5 min), and the supernatant solution was evaporated to remove the ethanol for ICP-MS measurement.

General procedure for the photocatalytic hydrogen evolution experiments. MOF hybrids for photocatalytic hydrogen evolution were loaded in 20 ml septum-sealed glass vials filled with H_2O (10 ml). Phenol (100 mg) was added as a sacrificial reducing agent. The sample vials were capped and deoxygenated by bubbling with nitrogen for 30 min. The vials were then placed in front of a 400 nm LED with magnetic stirring. The hydrogen evolution reaction lasted 24 hs, after which the gas in the headspace of the vial was analysed by GC (GC7900) to determine the amount of hydrogen generated.

General procedure for the water oxidation experiments. MOF hybrids for photocatalytic water oxidation were loaded in 20 ml septum-sealed glass vials filled with H_2O (10 ml). For testing the WOR-MOF, $Na_2S_2O_8$ (100 mg) was added as the sacrificial oxidizing agent; for the LP–WOR-MOF, 8.5 mg of $Na_2S_2O_8$ or TCBQ were added as the sacrificial oxidizing agent. Sample vials were capped and deoxygenated by bubbling with nitrogen for 30 min. The vials were then placed in front of a 450 nm LED with magnetic stirring. The water oxidation reaction lasted for 16 hs, after which the gas in the headspace of the vial was analysed by GC (GC7900) to determine the amount of oxygen generated.

Standard catalytic test for overall water splitting. The LP–HER-WOR-MOF (10 ml) was placed in a 20 ml sealed container and degassed with N_2 for 30 min before being placed under an LED light. The gaseous products were monitored by GC equipped with a thermal conductivity detector (column, TDX-01 and 5 Å molecular sieves; oven temperature, 120 °C; carrier gas flow rate, 50 ml min^{-1}; amount of headspace gas injected, 400 µl) at various time points.

Preparation of the sample containing both the HER-MOF and WOR-MOF inside the liposome. To a 100 ml round-bottomed flask was added PC (1.71 ml, 10 mg ml^{-1}), Chol (291 µl, 10 mg ml^{-1}) and TCBQ (1 mg). The solvent was removed by rotary evaporation to leave a thin film on the wall of the flask. The flask was kept in vacuo overnight. The dried lipid film was then hydrated in the presence of the HER-MOF (1.71 mg, unmodified), the WOR-MOF (1.71 mg) and $FeCl_3$ (1.5 mg). The mixture was sonicated for 10 min, followed by ten freeze–thaw cycles using liquid N_2 and then immersed in a 55 °C water bath to form a multilamellar vesicle suspension. The suspension was cooled slowly to room temperature over 30 min before being extruded with a mini-extruder at room temperature using a polycarbonate membrane (pore size 1 µm) for 11 cycles to obtain the liposomal assembly.

Determining the quantum yield of photocatalytic water splitting. The photocatalytic water-splitting reaction under the optimized conditions was carried out in a septum-sealed cuvette under N_2. The excitation light was from the Xe lamp on a fluorimeter with a grating monochromator. The excitation wavelength of the fluorimeter was set to 430 nm, and the reaction proceeded for 24 h before analysing the headspace gas using GC. The amount of hydrogen generated during the 24 h was calculated to be 0.2 µmol based on the GC data. The light intensity of the fluorimeter at 436 nm was then determined using potassium ferrioxalate as a chemical actinometer[52,52]. These measurements led to an apparent quantum yield of 2.5% for the water splitting.

The apparent quantum efficiency (AQE) was calculated using the following equation:

$$\mathrm{AQE} = \frac{N_e}{N_p} \times 100\% = \frac{4 \times n_{H_2} \times N_A \times h \times c}{S \times P \times t \times \lambda} \times 100\%$$

where N_p is the total number of incident photons, N_e is the total number of reactive electrons, n_{H_2} is the amount of H_2 molecules generated, N_A is Avogadro's constant, h is the Planck constant, c is the speed of light, S is the irradiation area, P is the intensity of irradiation light, t is the photoreaction time and λ is the wavelength of the monochromatic light.

General experimental. Commercial sources of all chemicals and experimental details of the ^{1}H NMR, TGA, ICP-MS, PXRD and TEM procedures can be found in the Supplementary Information.

Data availability

Source data are provided with this paper. All of the data that support the findings of this study, including catalytic measurements, material characterizations and spectroscopic data, are available within the paper and its Supplementary Information files. Further requests about the data can be directed to the corresponding author.

References

51. Jiang, Y. et al. Simulating powder X-ray diffraction patterns of two-dimensional materials. *Inorg. Chem.* **57**, 15123–15132 (2018).
52. Hatchard, C. G. & Parker, C. A. A new sensitive chemical actinometer - II. Potassium ferrioxalate as a standard chemical actinometer. *Proc. R. Soc. Lond. A* **235**, 518–536 (1956).

Acknowledgements

We acknowledge funding support from the Ministry of Science and Technology of China (2016YFA0200702) and the National Natural Science Foundation of China (no. 21671162 and no. 21721001). We acknowledge R. Huang and S. Zhang, B. Xu, Q. Wang, D. Guo and Y. Jiang for experimental help.

Author contributions

H.H. and C.W. conceived and designed this project. H.H. carried out the synthesis of the materials, characterized the materials and analysed the data. L.C. helped with the data analysis and structural determination. H.H. also performed the catalysis study. Z.W. and C.Z. performed the transient absorption experiments and data analysis. L.Z. performed elemental analysis. H.H., C.W. and W.L. wrote the manuscript. All the authors discussed the results and commented on the manuscript.

Competing interests

The authors declare no competing interests.

Additional information

Supplementary information is available for this paper at https://doi.org/10.1038/s41557-020-00635-5.

Correspondence and requests for materials should be addressed to C.W.

Reprints and permissions information is available at www.nature.com/reprints.